

On Accurate and Robust Estimation of 3D and 2D Circular Center: Method and Application to Camera-Lidar Calibration

Jiajun Jiang, Xiao Hu*, Wancheng Liu, and Wei Jiang

Abstract—Circular targets are widely used in LiDAR-camera extrinsic calibration due to their geometric consistency and ease of detection. However, achieving accurate 3D–2D circular center correspondence remains challenging. Existing methods often fail due to decoupled 3D fitting and erroneous 2D ellipse-center estimation. To address this, we propose a geometrically principled framework featuring two innovations: (i) a robust 3D circle center estimator based on conformal geometric algebra and RANSAC; and (ii) a chord-length variance minimization method to recover the true 2D projected center, resolving its dual-minima ambiguity via homography validation or a quasi-RANSAC fallback. Evaluated on synthetic and real-world datasets, our framework significantly outperforms state-of-the-art approaches. It reduces extrinsic estimation error and enables robust calibration across diverse sensors and target types, including natural circular objects. Our code will be publicly released for reproducibility.

Index Terms—Automatic calibration, extrinsic parameters, LiDAR, monocular cameras, stereo cameras.

I. INTRODUCTION

USING Light Detection and Ranging (LiDAR) and camera data is critical for robust perception in autonomous systems. This approach combines LiDAR’s precise 3D geometry with the rich photometric detail from 2D imagery. This sensor fusion benefits key downstream tasks, including multimodal 3D object detection [1], [2], semantic segmentation [3], and SLAM [4]. However, achieving spatially coherent data alignment requires precise extrinsic calibration: the estimation of the 6-degree-of-freedom (DoF) rigid transformation between sensor coordinate frames.

Decades of research in multi-sensor calibration have yielded a diverse array of methodologies for extrinsic parameter estimation, broadly categorized into target-based and target-less paradigms. Target-based approaches typically employ geometric or semantic meaningful targets, such as checkerboards [5]–[7], spheres [8]–[10], or patterned boards [11]–[20], to establish cross-modal correspondences through detectable features. In contrast, targetless calibration methods address in-field

This work was supported in part by the National Natural Science Foundation of China under Grant T2422002. (Corresponding author: Xiao Hu.)

Jiajun Jiang is with the Thrust of Robotics and Autonomous Systems, The Hong Kong University of Science and Technology (Guangzhou), 511453, China (email: jjjiang127@connect.hkust-gz.edu.cn).

Xiao Hu is with the Lower Airspace Economy Research Institute, International Digital Economy Academy, ShenZhen, 510085, China (e-mail: huxiao1@idea.edu.cn).

Wancheng Liu is with the Horizon-Continental Technology Corporation, Shanghai, 201800, China (email: wancheng.liu@horizon-continental.com).

Wei Jiang is with the State Key Laboratory of Rail Traffic Control and Safety and the Beijing Engineering Research Center of EMC and GNSS Technology for Rail Transportation, School of Electronic and Information Engineering, Beijing Jiaotong University, Beijing 100044, China (e-mail: weijiang@bjtu.edu.cn).

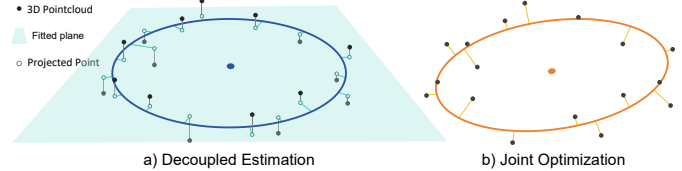


Fig. 1: Comparison of 3D circle fitting approaches. Decoupled fitting [37] estimates a plane first, then fits a 2D circle on projected points. Joint optimization [11], [38] simultaneously minimizes point-to-plane and point-to-circle distances.

calibration drift by leveraging environmental geometric [21]–[24], semantic [25]–[28], motion features [29], [30], or learned representations [31]–[36], without requiring physical targets. Target-based methods generally achieve superior accuracy and stability, but they require deliberately designed targets or set-ups, thus lacking operational flexibility. In contrast, targetless methods offer greater flexibility, especially for online recalibration. However, these methods risk instability or catastrophic decalibration [30], particularly in environments with sparse or ambiguous cross-modal correspondences [15], [18], [27], [30]. Consequently, to ensure robust and precise alignment, target-based methods remain indispensable for high-precision tasks, such as end-of-line production calibration and generating ground-truth data for targetless models.

Among calibration targets used in target-based calibration approaches, circular patterns, including circular holes [12], [13], [15]–[20] and circular board [11], [14], high-reflectivity circular tape, and sphere [8]–[10], have become predominant in offline LiDAR-camera calibration due to their exceptional occlusion resilience and cross-modal detection fidelity, as rigorously established in literature [11], [39], [40]. Despite these advantages, precisely localizing the 3D circle center (in LiDAR) and its corresponding 2D projection (in imagery) remains the primary error source in these calibration pipelines. This “Circle Center Problem” presents two critical challenges: First, extracting the 3D center from sparse LiDAR data is often compromised by conventional methods [13], [14], [17], [18], [20], [37]. These methods decouple 3D circle fitting into uncorrelated subproblems (e.g., plane segmentation followed by 2D fitting, see Fig. 1), which is geometrically inaccurate [11], [38]. Second, the 2D projection of the 3D circle center is systematically misidentified. Many methods erroneously assume the 2D ellipse center represents this projection [12], [13], [15]. However, as shown in Fig. 2, these two points diverge under oblique viewing angles, introducing perspective errors that propagate directly into the extrinsic estimation.

To overcome the Circle Center Problem, we introduce a

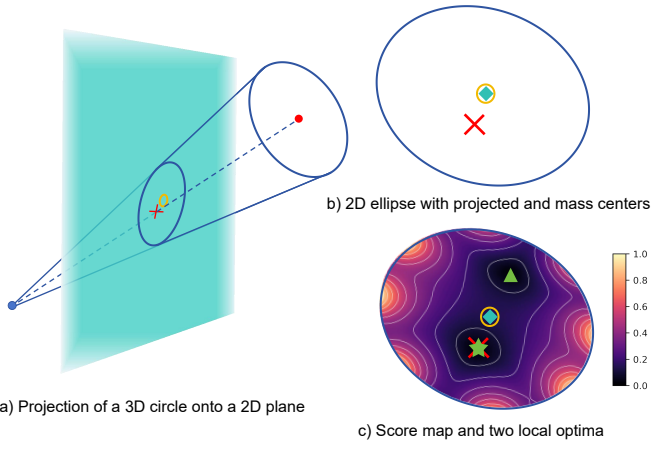


Fig. 2: Locating the true center of a 3D circle from its 2D image. (a) A circle in 3D space projects to an ellipse in the 2D image plane. (b) The key challenge: the point corresponding to the true 3D center (red cross) is displaced from the ellipse’s geometric center (yellow circle) and its center of mass (cyan diamond) due to perspective. (c) Our proposed score map optimization locates the true center (green star) and successfully disambiguates it from a false positive candidate (green triangle).

mathematically principled framework with two interlocking innovations: First, we apply Conformal Geometric Algebra (CGA) for 3D circle fitting [38]. CGA linearizes this nonlinear problem by transforming geometric distances into inner products in conformal space. This allows the 3D circle parameters (center, normal, and radius) to be solved simultaneously and efficiently via eigenvalue decomposition. This approach is inherently RANSAC-compatible, directly addressing the geometric inadequacy of classical decoupled solutions. Second, to recover the true 2D projected center, we propose a chord-length variance minimization method [41], [42], based on the geometric principle that unprojected chords of a circle must have equal length. While this optimization effectively finds the center, it suffers from a dual-minima ambiguity which the loss function alone cannot resolve. We resolve this ambiguity using a robust, dual-validation strategy. (i) If co-planar circles are available, we use a homography-based validation to definitively identify the correct minimum. (ii) When such geometry is absent, we introduce a quasi-RANSAC fallback that iteratively samples minima combinations to find the set yielding the lowest calibration reprojection error. Extensive synthetic and real-world experiments validate that our approach accurately localizes both 3D and 2D centers, achieving high-precision extrinsic calibration.

The primary contributions of this work are:

- This work solves robust 3D point cloud fitting via CGA formulation and RANSAC. Meanwhile, this work corrects 2D perspective distortion through chord-length standard deviation minimization, resolving local minima using multi-circle geometric constraints.
- Extensive experiments on synthetic and real-world

datasets validate the superior accuracy on 3D/2D center estimation and calibration over state-of-the-art approaches.

- An open-source implementation of the proposed framework to ensure reproducibility and facilitate community adoption.

The rest of this paper is organized as follows. Section II reviews related work on LiDAR-camera calibration and geometric fitting. Section III details our methodology for 3D and 2D circle center localization. Section IV presents the experimental setup and evaluation. Finally, Section V concludes the paper and discusses future work.

II. RELATED WORK

A. LiDAR-Camera Calibration

LiDAR-camera extrinsic calibration methods are broadly categorized as target-based or targetless. Target-based methods rely on predefined objects, such as checkerboards [5]–[7], spheres [8]–[10], or custom fiducial patterns [12]–[19], to establish geometric correspondences. These approaches typically yield high accuracy by optimizing point-to-point, point-to-edge, or point-to-plane distances via nonlinear optimization. In contrast, targetless methods circumvent the need for calibration objects. Earlier approaches exploited natural scene features like edges [22], [23], [25], intensity correlations [26], or motion cues from hand-eye calibration frameworks [29], [30]. More recently, deep learning has driven new solutions. Many employ depth estimation networks to create pseudo-dense depth maps from images, fusing them with LiDAR data to regress extrinsics end-to-end [31]–[34]. Other modern methods use semantic/geometric feature matching [24], [27], [28] or neural fields, where LiDAR and camera data reconstruct density and color fields, respectively [35], [36]. Despite these advances, targetless methods often struggle with generalization to new scenes and require substantial training data [43]. Crucially, they still rely on high-precision target-based calibration to generate ground-truth data for training and verification [15], [30]. This dependence confirms the critical need for accurate and robust target-based methods, which is the focus of our work.

B. Calibration Using Circular Patterns

Circular targets are broadly categorized into 3D spherical targets and 2D planar targets. Spherical targets offer view-invariant symmetry and have been used for robust center estimation from ellipse contours [8]–[10]. However, planar boards with circular patterns (e.g., holes) are more widely adopted, as they provide robust features in sparse LiDAR point clouds [11], [40]. These boards range from simple hole arrays to hybrid designs integrating fiducial markers like ArUco [13], [15]–[18], checkerboards [19], or encoded patterns [12]. Despite their widespread use, existing methods for localizing these circular centers suffer from fundamental geometric inaccuracies, which we defined in the introduction as the “Circle Center Problem”.

3D Center Estimation. Most methods extract 3D centers using a decoupled sequential process: fitting a plane, projecting

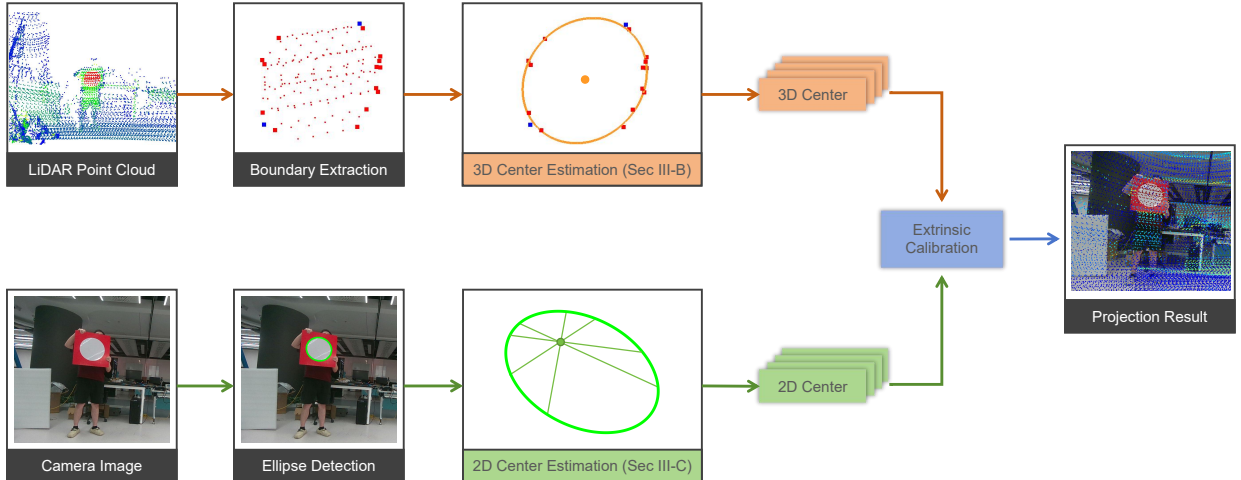


Fig. 3: Overview of the LiDAR-Camera calibration pipeline. The primary contributions—robust 3D circle fitting via CGA and perspective-aware 2D center refinement—enable accurate 3D-2D correspondences for high-precision extrinsic calibration.

points onto it, and performing 2D circle fitting [13], [14], [17], [18], [20]. This approach is geometrically flawed, as it does not minimize the true 3D point-to-circle distances [11]. While refinements like template matching [19] or edge optimization [15], [16] exist, they do not address the underlying geometric inaccuracy of the decoupled fitting. **2D Projected Center Estimation.** Accurately finding the 2D projection of the 3D center is equally challenging. Current approaches typically fall into two categories, both problematic: (1) erroneously assuming the 2D ellipse (or blob) center is the true projected center [12], [13], [15], which ignores perspective distortion (as shown in Fig. 2); or (2) projecting the 3D center using a pose derived from other features (e.g., ArUco or checkerboard corners) [14], [16]–[19]. This second approach merely transfers the error source, making the circle center’s accuracy dependent on a separate, and potentially error-prone, pose estimation. Overall, accurately localizing the circular center in both 3D and 2D remains an overlooked issue that fundamentally limits calibration accuracy. Our work is designed to resolve this gap.

III. METHOD

In this paper, we maintain a consistent notation system: matrices are denoted by boldface capital Roman letters, vectors by boldface lowercase Roman letters, and scalars by standard lowercase letters. Variables in conformal space are represented using capital letters. For special cases, both zero matrices and zero vectors are denoted by $\mathbf{0}$, while the symbol \mathbf{I} is reserved exclusively for identity matrices.

A. Overview

We assume the intrinsic calibration parameters of the camera and the LiDAR are known, and we focus only on the extrinsic parameters for LiDAR–camera systems. We adopt a camera–lidar calibration pipeline depicted in Fig. 3. As our primary contribution in this work lies in the estimation of 3D and 2D circle centers, which are further utilized to establish 3D–2D correspondences and perform extrinsic estimation. In the

following sections, we will mainly introduce these primary contributions. First, we briefly describe our solutions for the LiDAR and image feature preprocessing modules.

The LiDAR feature preprocessing module takes the point cloud captured by the LiDAR as its input. Its output is a list of boundary points that will be used for circle fitting. To obtain this output, distance and reflectance filtering are applied to segment the points of interest from the raw point cloud. Subsequently, distance clustering is employed to identify clusters of suitable size. Boundary points can then be extracted based on depth discontinuities for scanning LiDAR [18] or directional gap among its neighbors [16].

The image feature preprocessing module uses the corresponding image captured by the camera as its input. Due to the perspective effect, the projection of a 3D circle is typically an ellipse. Thus, the output of this module is a list of detected ellipses. For ellipse detection, we recommend using SOTA arc-based approaches [44], [45]. These approaches have demonstrated superior performance compared to hough transform based methods [46], [47], as shown in numerous studies [44], [45], [48].

For extrinsic calibration between the LiDAR and camera, we employ the Perspective-n-Point (PnP) algorithm, which estimates the 6-DOF rigid transformation \mathbf{T}_L^C mapping points from the LiDAR frame to the camera frame. This requires correspondences between known 3D LiDAR points $\{\mathbf{p}_i^L\}_{i=1}^n$ and their projected 2D image points $\{\mathbf{q}_i^C\}_{i=1}^n$, which is detailed in Section III-B and Section III-C, respectively. Once these 3D-2D point pairs are found, the transformation \mathbf{T}_L^C is then computed by minimizing the re-projection error:

$$\mathbf{T}_L^C = \arg \min_{\mathbf{T}_L^C} \sum_{i=1}^n \|\mathbf{q}_i^C - \pi(\mathbf{T}_L^C \mathbf{p}_i^L)\|_2, \quad (1)$$

where $\pi()$ represents the projection.

B. 3D Center Estimation

To robustly estimate the 3D circle parameters—center \mathbf{c} , normal \mathbf{n} , and radius r —from noisy boundary points $\mathbf{p}_i \in$

\mathbb{R}^3 , $i = 1, 2, \dots, n$, we propose a CGA-based estimator integrated within a RANSAC framework. Unlike classical decoupled approaches, i.e., plane fitting followed by 2D fitting, the proposed method jointly models the circle as a geometric primitive in conformal space, enabling direct minimization of geometric distance rather than algebraic proxies. This leads to significantly improved accuracy under noise and partial occlusion, as validated in [Section IV-A1](#). Furthermore, by embedding this analytical solver into RANSAC [\[49\]](#), our approach gains strong resilience to outliers without sacrificing efficiency.

CGA extends Euclidean space \mathbb{R}^3 into a 5D Minkowski space $\mathbb{R}^{4,1}$ [\[50\]](#), spanned by an orthonormal basis $\{\mathbf{e}_1, \mathbf{e}_2, \mathbf{e}_3, \mathbf{e}_+, \mathbf{e}_-\}$, where $\mathbf{e}_+^2 = 1, \mathbf{e}_-^2 = -1$, and $\mathbf{e}_+ \cdot \mathbf{e}_- = 0$. For geometric clarity, it is often convenient to reparameterize this space using the null basis:

$$n_0 = \frac{1}{2}(\mathbf{e}_- + \mathbf{e}_+), \quad n_\infty = \mathbf{e}_- - \mathbf{e}_+, \quad (2)$$

satisfying $n_0 \cdot n_0 = n_\infty \cdot n_\infty = 0$ and $n_0 \cdot n_\infty = -1$. A 3D point $\mathbf{p} = (x, y, z)$ is mapped to its conformal representation:

$$P = \mathbf{p} + n_0 + \frac{1}{2}\|\mathbf{p}\|^2 n_\infty \quad (3)$$

where n_0 encodes the origin and n_∞ represents the point at infinity. Crucially, the squared Euclidean distance between two points \mathbf{p}, \mathbf{q} is recovered via the inner product of their conformal counterparts:

$$P \cdot Q = -\frac{1}{2}\|\mathbf{p} - \mathbf{q}\|^2. \quad (4)$$

This linearizes distance computation—a foundational advantage for algebraic optimization. In CGA space, a 3D circle CC is represented as the outer product (\wedge) of a sphere SP and a plane PL :

$$\begin{aligned} SP &= C - 0.5\rho^2 n_\infty, \\ PL &= \mathbf{n} + \delta n_\infty, \\ CC &= SP \wedge PL. \end{aligned} \quad (5)$$

Here, SP represents the conformal entity for a sphere centered at \mathbf{c} with radius ρ . PL represents a plane with normal \mathbf{n} and offset δ . A point P lies on CC if and only if it satisfies both $P \cdot SP = 0$ and $P \cdot PL = 0$. To measure the distance from a point P to the circle CC , we use the scalar-valued expression derived from the metric structure of CGA [\[38\]](#):

$$-\frac{(P \cdot CC) * (P \cdot CC)}{CC * CC} = \frac{(P \cdot SP)^2}{SP^2} + \frac{(P \cdot PL)^2}{PL^2}. \quad (6)$$

where $*$ denotes the scalar product. This measure in [\(6\)](#) provides a geometrically meaningful cost function: the first term approximates the deviation from the spherical constraint, while the second enforces exact planar alignment. Unlike algebraic errors used in many direct estimation methods, this cost reflects the true spatial relationship between the point and the circle. Therefore, to fit a circle to n noisy 3D points $\{\mathbf{p}_i\}$, we minimize the sum of approximate squared distances from points to the circle, which can be written as

$$\mathcal{L}(CC) = \frac{1}{n} \sum_{i=1}^n \frac{(P_i \cdot CC) * (P_i \cdot CC)}{CC * CC}. \quad (7)$$

Crucially, this optimization can be solved analytically via eigen-decomposition of an inertial matrix \mathbf{P} . Let's define the data matrix as:

$$\mathbf{D} = \begin{bmatrix} \mathbf{p}_1 & \dots & \mathbf{p}_N \\ 1 & \dots & 1 \\ \frac{1}{2}\|\mathbf{p}_1\|^2 & \dots & \frac{1}{2}\|\mathbf{p}_N\|^2 \end{bmatrix}, \quad (8)$$

and the metric tensor:

$$\mathbf{M} = \begin{bmatrix} \mathbf{I}_3 & \mathbf{0} & \mathbf{0} \\ \mathbf{0}^\top & 0 & -1 \\ \mathbf{0}^\top & -1 & 0 \end{bmatrix}, \quad (9)$$

the optimal circle is encoded in the eigenvectors V, U corresponding to the two smallest nonnegative eigenvalues of $\mathbf{P} = \frac{1}{n}\mathbf{D}\mathbf{D}^\top\mathbf{M}$. Let $V, U \in \mathbb{R}^5$ be these two eigenvectors. Their outer product yields the dual bivector representation of the circle:

$$E = V \wedge U = \begin{bmatrix} [\mathbf{v}^\times] & \mathbf{0} & \mathbf{0} \\ v_0 \mathbf{I}_3 & -\mathbf{v} & \mathbf{0} \\ -v_\infty \mathbf{I}_3 & \mathbf{0} & \mathbf{v} \\ \mathbf{0}^\top & -v_\infty & v_0 \end{bmatrix} \begin{bmatrix} \mathbf{u} \\ u_0 \\ u_\infty \end{bmatrix}. \quad (10)$$

The circle parameters are then extracted from E using closed-form formulas:

$$\begin{aligned} \mathbf{n} &= -E_{3,4,5}, & \mathbf{c} &= (\mathbf{K}\mathbf{n})/\|\mathbf{n}\|^2, \\ r^2 &= \|\mathbf{c}\|^2 - 2\mathbf{n} \cdot E_{6,7,8} - 2(\mathbf{c} \cdot \mathbf{n})^2, \end{aligned} \quad (11)$$

where E_i denotes the i -th component of E in the ordered basis $\{\mathbf{e}_1, \mathbf{e}_2, \mathbf{e}_3, n_0, n_\infty\}$, and \mathbf{K} is the 3×3 matrix defined as $\mathbf{K} = -E_9\mathbf{I} + [E_1, E_2, E_3]^\top$. This entire process requires only one eigen-decomposition and no iterative optimization, yielding a fast and deterministic fit. For a rigorous derivation, we refer the reader to read [\[38\]](#). The fitting accuracy of our CGA-based estimator is thoroughly validated in [Section IV](#), where we demonstrate superior performance over classical decoupled methods implemented in PCL—particularly under high noise levels and partial occlusion, where traditional approaches suffer from error accumulation due to sequential plane and 2D fitting.

It is inevitable that real-world point clouds contain outliers arising from sensor noise, occlusions, or spurious detections. While our CGA estimator excels in noisy but inlier-dominated scenarios, robustness to gross outliers is essential for deployment in unstructured environments. Fortunately, because our solution reduces circle fitting to a linear eigenvalue problem, similar in structure to the eight-point [\[51\]](#) and five-point [\[52\]](#) algorithms for essential matrix estimation, it integrates seamlessly with RANSAC [\[49\]](#). To construct our RANSAC framework, we leverage three key components:

- 1) **Minimal sample size:** 5 points, sufficient to uniquely determine \mathbf{P} via [\(8\)](#) and [\(9\)](#);
- 2) **Model computation:** Fast, closed-form circle estimation via eigendecomposition;
- 3) **Inlier scoring:** Geometric distance metric [\(6\)](#), which accurately reflects spatial alignment with the true circle.

This design inherits the speed and stability of CGA while gaining outlier rejection capability. Compared to decoupled methods implemented in PCL, our RANSAC-CGA pipeline

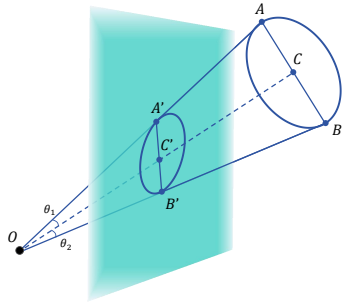


Fig. 4: Geometric constraint under projection

demonstrates superior resilience to both noise and partial occlusion—critical for robotic perception tasks involving incomplete or corrupted sensor data.

C. 2D Center Estimation

At this stage, we are given a set of detected ellipses in the image, each parameterized by a conic matrix $\mathbf{Q} \in \mathbb{R}^{3 \times 3}$ such that a point $\mathbf{p} = [u, v, 1]^\top$ lies on the ellipse if $\mathbf{p}^\top \mathbf{Q} \mathbf{p} = 0$, where

$$\mathbf{Q} = \begin{bmatrix} Q_{11} & Q_{12} & Q_{13} \\ Q_{21} & Q_{22} & Q_{23} \\ Q_{31} & Q_{32} & Q_{33} \end{bmatrix}, \quad (12)$$

where Q_{ij} denotes the coefficient of the conic. While the geometric center of an ellipse in image space is often naively assumed to be the projection of the 3D circle's center [12], [13], [15], this is invalid in practice due to perspective projection [41], [42], [53]. As the calibration accuracy relies on the precision of 2D projection center, we therefore seek the true projected 3D circle center $\mathbf{c} \in \mathbb{R}^2$ that best corresponds to the underlying 3D geometry.

Inspired by [42], we exploit the following key insight: if \mathbf{c} is the true projection of a 3D circle center, then every chord passing through \mathbf{c} in the image must correspond to a diameter in 3D space. Consequently, the distance from the camera center to the circular plane, calculated using trigonometry from the chord and \mathbf{c} using trigonometry should exhibit zero variance. To quantify this, a loss function can be defined based on the variation of the recovered distances, computed over multiple candidate directions. As shown in Fig. 4, given a candidate center \mathbf{c} and an ellipse \mathbf{Q} , we sample n lines passing through \mathbf{c} at uniformly spaced angles γ_i . Each line intersects the ellipse at two points $\mathbf{a}_i, \mathbf{b}_i$, whose deprojected rays in 3D (via inverse camera projection $\mathbf{r}_u = \mathbf{K}^{-1} \tilde{\mathbf{u}} / \|\mathbf{K}^{-1} \tilde{\mathbf{u}}\|$ where $\tilde{\mathbf{u}}$ is the homogeneous coordinate of \mathbf{u}) form a chord of the unknown 3D circle. Using the law of cosines on the viewing rays and the known circle radius r , we compute the distance $d_i = \|OC\|$ from the camera center O to the 3D circle center C ($s(\cdot)$ and $c(\cdot)$ are used to denote \sin and \cos):

$$d_i = \frac{\sqrt{2}rs(\theta_{i1} + \theta_{i2})}{\sqrt{3 - 2c(2\theta_{i1}) - 2c(2\theta_{i2}) + c(2(\theta_{i1} + \theta_{i2}))}}, \quad (13)$$

where $\theta_{i1} = \cos^{-1}(\mathbf{r}_{a_i} \cdot \mathbf{r}_c)$ and $\theta_{i2} = \cos^{-1}(\mathbf{r}_{b_i} \cdot \mathbf{r}_c)$ are the angular separations between the viewing rays and the

candidate center direction. If \mathbf{c} is correct, all d_i must be equal, which yields minimal variance. We thus minimize:

$$\mathcal{L}(c) = \frac{1}{n} \sum_{i=1}^n (d_i - \mu_d)^2, \quad \mu_d = \frac{1}{n} \sum_{i=1}^n d_i. \quad (14)$$

Namely, for a given ellipse, we search for \mathbf{c} for which the dispersion of the values of d is minimized. Unlike [42], we avoid using the standard deviation to preserve smoother differentiability. However, this loss function typically exhibits two local minima within the ellipse with only one corresponding to the true center. Without additional constraints, these minima are indistinguishable based on the loss alone, a limitation not resolved in [42]. In the following, we show that we could resolve this ambiguity using a second co-planar, non-concentric ellipse. The key observation is that a correct center enables a *canonical rectifying homography* \mathbf{H} that transforms the ellipse into a circle centered at the origin, recovering the Euclidean geometry of the plane up to similarity (rotation and scaling) [53]. Crucially, if the candidate center \mathbf{c} is incorrect, for instance, when using the ellipse's geometric center as the projection center, the homography \mathbf{H} still maps the associated ellipse to a circle, but it distorts the Euclidean geometry of the plane. As a result, while individual ellipses are rectified to circles, the relative scale between two co-planar, non-concentric ellipses is no longer preserved under \mathbf{H} , making it possible to distinguish the true center.

Specifically, given a candidate center \mathbf{c}' , we first apply an affine transformation $\mathbf{T} = \mathbf{A}_1 \mathbf{A}_2$ to center and rotate the ellipse into canonical form:

$$\mathbf{A}_1 = \begin{bmatrix} \cos \theta & \sin \theta & 0 \\ -\sin \theta & \cos \theta & 0 \\ 0 & 0 & 1 \end{bmatrix}, \quad (15)$$

$$\mathbf{A}_2 = \begin{bmatrix} 1 & 0 & -e_x \\ 0 & 1 & -e_y \\ 0 & 0 & 1 \end{bmatrix}$$

where (e_x, e_y) is the ellipse center and θ the ellipse's orientation. The transformed conic becomes simplified:

$$\mathbf{Q}' = (\mathbf{T}^{-1})^\top \mathbf{Q} \mathbf{T}^{-1} = \begin{bmatrix} Q_{11} & 0 & 0 \\ 0 & Q_{22} & 0 \\ 0 & 0 & -1 \end{bmatrix} \quad (16)$$

The rectifying homography $\mathbf{H} = \mathbf{H}_e \mathbf{H}_a \mathbf{H}_p$ is then constructed as:

$$\mathbf{H}_p = \begin{bmatrix} 1 & 0 & 0 \\ 0 & 1 & 0 \\ Q'_{11} c'_x & Q'_{22} c'_y & Q'_{33} \end{bmatrix}, \quad (17)$$

$$\mathbf{H}_a = \begin{bmatrix} 1/b & -a/b & 0 \\ 0 & 1 & 0 \\ 0 & 0 & 1 \end{bmatrix}, \quad \mathbf{H}_e = \begin{bmatrix} 1 & 0 & x \\ 0 & 1 & y \\ 0 & 0 & 1 \end{bmatrix},$$

with parameters a, b, x, y derived from Q'_{ij} and the transformed center $[c'_x, c'_y, 1]^\top = \mathbf{T}[c_x, c_y, 1]^\top$ as follows:

$$\begin{aligned} a &= \frac{Q'_{22}c'_x c'_y}{Q'_{11}c'_x^2 + Q'_{33}}, \\ b &= \sqrt{\frac{Q'_{22}Q'_{33}}{Q'_{11}} \cdot \frac{Q'_{11}c'_x^2 + Q'_{22}c'_y^2 + Q'_{33}}{(Q'_{11}c'_x^2 + Q'_{33})^2} - a^2}, \\ x &= \frac{-c'_x/b + c'_y a/b}{Q'_{11}c'_x^2 + Q'_{22}c'_y^2 + Q'_{33}}, \\ y &= \frac{-c'_y}{Q'_{11}c'_x^2 + Q'_{22}c'_y^2 + Q'_{33}}. \end{aligned} \quad (18)$$

Applying \mathbf{H} to coplanar ellipses maps them to the rectified plane. If c is the true projection center, the ratio of their radii is preserved under similarity. Thus, we use the ratio consistency between the two rectified circles as a discriminator: the candidate center c that yields the closest match to the known physical radius ratio \hat{r}_1/\hat{r}_2 is selected as the true 3D projection center. We evaluate the effectiveness in [Section IV](#).

D. Practical Solution in the Absence of Coplanar Circles

In practical scenarios, coplanar circles may not always be available, as observed in our experiments ([Section IV](#)). To enhance the applicability, we now propose a robust fallback strategy that enables calibration even when no such geometric constraint exists. For each detected ellipse, we optimize the 2D center loss function (14) using grid search or iterative optimization to identify both candidate centers corresponding to the two local minima. This yields $2n$ potential 2D centers. Since no additional geometric constraint is available to distinguish the true from spurious candidates, we integrate these ambiguities directly into a modified RANSAC framework for PnP. Unlike standard RANSAC, which randomly samples point correspondences, our approach samples candidate pairs: for each selected 3D point, we randomly choose one of its two 2D hypotheses. We iteratively construct pose hypotheses by sampling k such ambiguous correspondences and evaluate the re-projection error. The hypothesis with the lowest cumulative error is retained. This procedure effectively explores the combinatorial space of candidate correspondences in practice. As demonstrated in [Section IV](#), this approach significantly improves success rate over naive selection strategies, enabling reliable calibration in unstructured environments where coplanar features are absent.

IV. EXPERIMENTS

A. Numerical Experiments

1) *Evaluation on 3D Circle Estimation:* To rigorously evaluate the performance of our CGA-based 3D circle fitting method, we design two comprehensive synthetic benchmarks against the widely adopted PCL implementation [37], which uses a decoupled plane + 2D circle fitting strategy. Our experiments are structured to assess performance under four challenging conditions affecting accuracy (noise, partial coverage, sparsity) and one dedicated test for outlier robustness, mirroring real-world scenarios in robotic perception, such

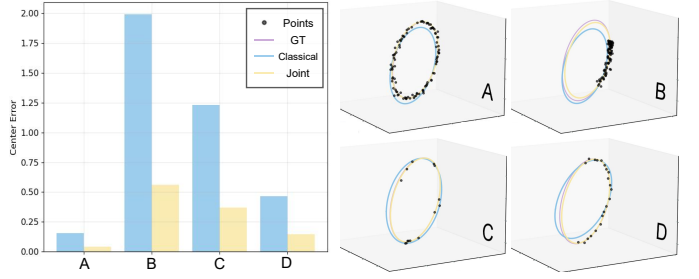


Fig. 5: Comparison results of Accuracy Under Challenging Geometric Conditions.

TABLE I: Comparison of PCL and CGA Methods Across Outlier Proportions

Method	Outlier Proportion				
	10%	20%	30%	40%	50%
PCL	0.0817	0.0870	0.0826	0.0775	0.0777
CGA	0.0354	0.0347	0.0356	0.0362	0.0364

as LiDAR-based calibration or circular feature detection in industrial inspection.

a) *Accuracy Under Challenging Geometric Conditions:* We conduct a Monte Carlo study with 1000 independent trials per scenario, each using randomly generated ground-truth circles defined by: $\mathbf{c}_{gt} \sim \mathcal{U}(-2, 2)^3$, $r_{gt} \sim \mathcal{U}(1, 5)$, $\mathbf{n}_{gt} \sim \mathcal{N}(0, \mathbf{I}_3)$. For each trial, points are sampled on the true circle and corrupted with isotropic Gaussian noise $\mathcal{N}(0, \sigma^2)$ with $\sigma = 0.2$, unless otherwise specified. We evaluate four distinct configurations:

- **A - Full Circle + Isotropic Noise:** $N=100$ points are uniformly sampled over a full 360° spanned arc. Represents ideal conditions with dense, even sampling.
- **B - Partial Arc Coverage:** $N = 100$ points are sampled over a 70° arc with non-uniform angular density biased toward one end via power-law distribution, i.e., $\theta_i = u_i^2 \cdot \theta_{arc} - 0.2 \cdot \theta_{arc}$, $u_i \sim \mathcal{U}(0, 1)$. The purpose of this test is to assess the sensitivity to incomplete geometry when objects are partially occluded.
- **C - Sparse Clustered Points:** only $N = 12$ points distributed across 2-3 angular clusters. Each cluster is centered at a random angle with angular spread $\sigma_{cluster} \sim \mathcal{U}(\pi/30, \pi/9)$. This is to simulate low-resolution sensing or sparse edge detection.
- **D - Symmetric Sparse Arc:** $N = 20$ points distributed symmetrically over a 200° arc, with angular intervals drawn from $\mathcal{U}(0.8, 1.2)$ and normalized to span the arc. It is designed to mimic circular holes or rings where boundary points are detected only at discrete, symmetric locations.

For each configuration, we compute the center and radius estimation error as $E_c = \|\mathbf{c}_{est} - \mathbf{c}_{gt}\|_2$ and report mean and standard deviation across all 1000 trials.

b) *Outlier Robustness Evaluation:* To evaluate resilience to gross outliers - critical for deployment in unstructured environments, we generate 100 trials per outlier ratio level ($p \in \{0.1, 0.2, 0.3, 0.4, 0.5\}$), totaling 500 experiments. For

each trial in the outlier robustness evaluation, a complete 360° circle is generated with 100 uniformly sampled inlier points, to which isotropic Gaussian noise $\mathcal{N}(0, 0.1^2)$ is applied to simulate sensor measurement uncertainty. Outliers are then introduced by sampling $N_{\text{out}} = p \cdot N$ points randomly, where the outlier proportion p ranges from 0.1 to 0.5. The combined set of inliers and outliers is randomly shuffled to remove any spatial correlation or positional bias, ensuring that the fitting algorithm must rely solely on geometric structure rather than point ordering or clustering to distinguish true circle points from spurious measurements.

c) Results and Implementation Details: All methods are implemented in C++, with our CGA-RANSAC estimator compared directly against PCL’s (CIRCLE3D with SACMODEL) using identical input point clouds. For fair comparison, both RANSAC variants use a maximum iteration of 1000. As shown in Fig. 5 and Table I. It is evident that the CGA-RANSAC method consistently outperforms PCL across all conditions, especially under partial coverage. Under full coverage and noise, it achieves $\sim 60\%$ lower center error due to its geometrically grounded cost function. Under partial coverage and sparsity, PCL fails catastrophically, while CGA maintains $\sim \frac{1}{4}$ error.

2) Evaluation on 2D Circle Estimation: We conduct two Monte Carlo experiments (1,000 trials each) to evaluate the accuracy of our homography-based 2D center refinement method and its impact on extrinsic calibration. All simulations use a synthetic camera with intrinsic parameters $f_x = f_y = 600, c_x = 640, c_y = 480$. For each trial, we generate two coplanar, nonconcentric 3D circles: one as the primary circle (for center estimation) and one as the validation circle (to resolve ambiguity via radius-ratio consistency).

a) Accuracy of 2D Center Estimation: In the first experiment, we assess the precision of the estimated 2D projection of the primary circle’s center. 3D points are sampled uniformly on both circles, projected into the image plane, and corrupted by isotropic Gaussian noise ($\sigma = 1$ pixels). Ellipses are fitted to the noisy projections using least-squares conic fitting. We then search for the true 2D projection center by evaluating the chord-length variance loss (14) over a dense grid of pixel candidates centered on the ellipse’s geometric center. Non-maximum suppression identifies the two local minima in the loss map. We compare three types of center: 1) **Ellipse Center**; 2) **Center of Mass** as the first-order image moment of the elliptical region; and 3) **Proposed (Refined)** center via canonical homography. The true 2D projection of the 3D circle center, computed from the noise-free geometry and exact camera pose, is denoted as **Ground Truth** or GT for brevity. The 2D localization error $\Delta = [\Delta x, \Delta y]^\top = \|\mathbf{c}_{\text{est}} - \mathbf{c}_{\text{gt}}\|_2$ is computed for each method.

As shown in Fig. 6, our refined method achieves significantly lower mean error and tighter error distribution than baseline methods. While ellipse center and center-of-mass exhibit large biases and long tails, our method reduces mean error to approximately 1.27 pixel. We also note that some outliers persist due to the following reasons: (1) discretization from integer-pixel grid sampling, which may cause the true minimum to fall between pixels; and (2) noise-induced instability in the loss landscape, leading to spurious local minima

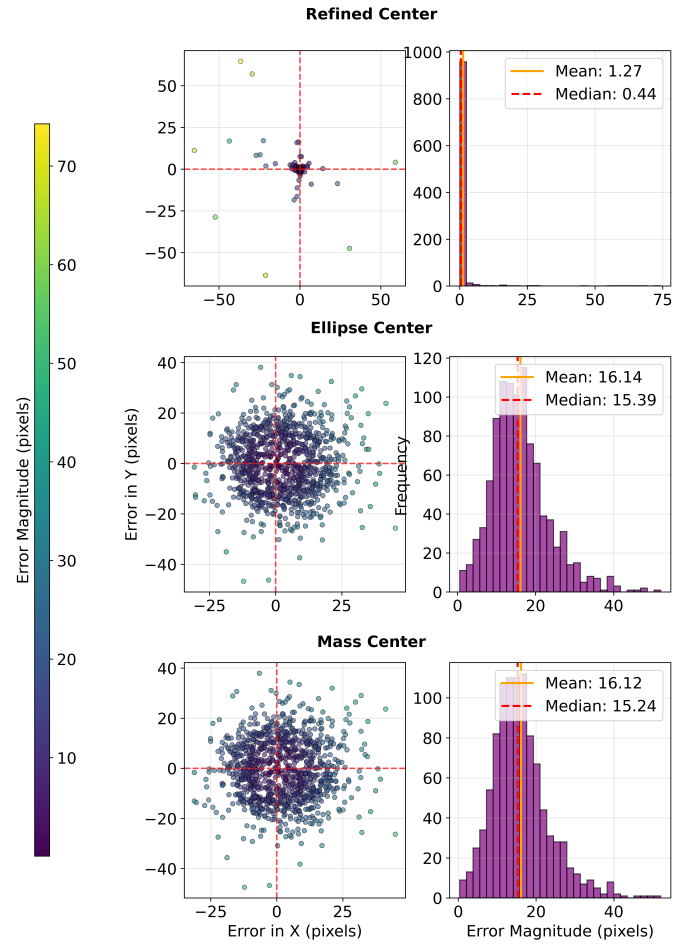


Fig. 6: Error distribution of 2D center estimated using different methods. The refined center using the proposed method achieves a lower mean error and a tighter distribution compared to the ellipse center and center of mass.

that are incorrectly selected over the true one. We will address these limitations in future work through sub-pixel optimization and robust loss weighting.

b) Impact on Pose Estimation Accuracy: In the second experiment, we evaluate how accurate 2D center estimation affects downstream pose estimation. For each trial, we generate 20 random 3D circle pairs, each consisting of a primary circle (used for pose estimation) and an alternative non-concentric circle (used to validation). Using the same four 2D center estimates as above, we run PnP-RANSAC with 1000 iterations to estimate the camera pose. We evaluate the performance of three 2D center estimation methods—ellipse center, center of mass, our refined estimates using homograph validation and proposed RANSAC-based validation—using three error metrics:

- **Reprojection Error:** $\epsilon_{\text{reproj}} = \frac{1}{n} \sum_{i=1}^n \|\pi(\mathbf{RP}_i + \mathbf{t}) - \mathbf{q}_i\|_2$.
- **Rotation Error:** $\epsilon_{\text{rot}} = \|\log(\mathbf{R}_{\text{gt}}^{-1} \mathbf{R}_{\text{est}})\|^\vee$.
- **Translation Error:** $\epsilon_{\text{trans}} = \|\mathbf{t}_{\text{est}} - \mathbf{t}_{\text{gt}}\|_2$.

Results, shown in Figure 7, demonstrate that using our refined 2D centers, both using homography validation and RANSAC,

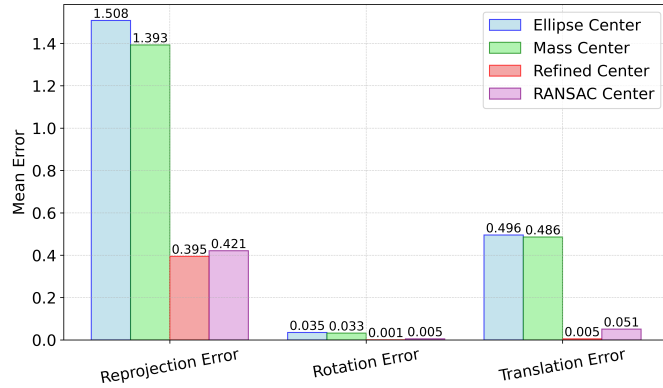


Fig. 7: Comparative analysis of pose estimation accuracy across different 2D center estimation methods. The results demonstrate that the refined center estimates, enhanced through homography validation or RANSAC, achieve substantial reductions in reprojection, rotation, and translation errors relative to baseline techniques.

leads to dramatically improved extrinsic calibration. Compared to ellipse-center or center-of-mass baselines, our method reduces median reprojection error, rotation error, and translation error significantly. These gains stem directly from the geometric fidelity of our refined correspondences, enabling PnP to converge to a more accurate and consistent solution.

B. Synthetic Experiments

To comprehensively evaluate the performance of the proposed method, we adopt the synthetic test suite introduced in [18], which leverages the Gazebo simulator [54] to generate realistic LiDAR–camera data. For details regarding sensor models and scene configuration, we refer the reader to [18]. The synthetic data are corrupted with additive Gaussian noise $\epsilon \sim \mathcal{N}(0, (K\sigma_0)^2)$ where the noise factor K controls the noise level: $K = 0$ corresponds to a noise-free setting, $K = 1$ to a realistic operating condition and $K = 2$ to a highly noisy scenario. In our experiments, we focus on the latter two cases to assess robustness under practical and challenging conditions.

Following the evaluation protocol of [18], we structure our experiments around three key aspects: (i) 3D reference point extraction accuracy, (ii) calibration performance using a single target pose, and (iii) multi-pose calibration accuracy. We denote the open-source implementation from [18] as *velo2cam* and our method as *proposed*.

1) *Single-Sensor Experiments*: Following the protocol in [18], we first evaluate the accuracy of 3D circular center estimation. The error is defined as the Euclidean distance between the estimated center and the ground-truth center of the calibration target. As shown in Fig. 8, the proposed method consistently achieves lower estimation errors in both realistic and noisy environments, demonstrating superior robustness to sensor noise and point cloud sparsity.

2) *Single & Multiple Pose Experiments*: We next evaluate the full extrinsic calibration pipeline. The accuracy of the

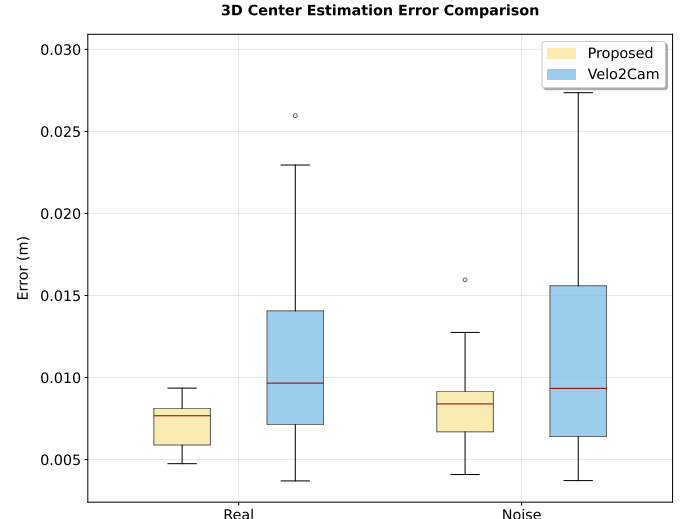


Fig. 8: 3D center estimation error comparison. The proposed CGA-based method (*proposed*) outperforms the baseline (*velo2cam* [18]) across realistic and noisy conditions.

TABLE II: Calibration Errors for Single- and Multi-Pose Configurations

Exp	$e_{\text{trans}} (\text{cm})$		$e_{\text{rot}} (10^{-2}\text{rad})$		
	velo2cam	proposed	velo2cam	proposed	
Single	P1	11.20	3.84 \downarrow	4.09	2.53 \downarrow
	P2	4.85	5.39 \uparrow	2.27	1.08 \downarrow
	P3	9.47	6.86 \downarrow	7.07	6.05 \downarrow
Multiple		5.54	3.88 \downarrow	0.69	0.32 \downarrow

estimated transformation is quantified using translation error (in cm) and rotation error (in radians), as defined in the previous section. We follow the *single-pose* and *multi-pose* experimental protocols from [18]. Results are summarized in Table II. In the multi-pose setting, the proposed method reduces translation error from 5.54 cm to 3.88 cm and rotation error from $0.69e^{-2}$ rad to $0.32e^{-2}$ rad, showing improvements of 30% and 54%, respectively. In the single-pose trials, our method consistently improves rotation accuracy and achieves lower translation error in two out of three poses (P1 and P3). The slight increase in translation error at P2 is offset by a significant reduction in angular error, indicating more geometrically consistent correspondences. These results confirm that the joint refinement of 3D and 2D circle centers leads to more accurate and robust extrinsic calibration, particularly when sensor data are noisy or the target is viewed from challenging viewpoints.

C. Real World Calibration

To assess practical robustness, we evaluate our method on real-world data from public datasets [16], [55] and two custom-collected setups. These experiments cover diverse targets, including planar boards, reflective markers, and natural objects. As ground-truth extrinsics are unavailable, we perform qualitative validation by projecting the LiDAR point cloud onto the image plane using the estimated transformation.



(a) Planar board target on [16] (b) Natural target on [55] (c) Collected data by Setup 1 (d) Collected data by Setup 2

Fig. 9: Qualitative results of LiDAR-camera calibration on real-world data. Top: RGB image. Bottom: LiDAR point cloud (colored by intensity) projected into the image using the estimated extrinsics. Precise alignment across diverse sensors and target types validates the robustness of the proposed method.



(a) Setup 1: Orbbec (pinhole) and Livox Mid360 (solid-state). (b) Setup 2: Insta360 (fisheye) and Hesai XT32 (mechanical).

Fig. 10: Our two custom-collected sensor setups used for evaluating robustness. (a) Pinhole camera and solid-state LiDAR. (b) Fisheye camera and mechanical LiDAR.

We first evaluate on the dataset from [16], which features planar targets and multiple LiDAR-camera configurations (e.g., Ouster OS1-128, Livox Avia) paired with a wide-angle camera. For brevity, Fig. 9a shows the accurate reprojection result for the Ouster configuration. To demonstrate applicability in unstructured environments, we also use Scene 2 from the [55] dataset. This scene features a bicycle wheel as an implicit circular target for a Livox Mid-70 LiDAR and a SENSING-GSML camera. Although our method is not designed specifically for natural objects, Fig. 9b confirms a coherent alignment using the wheel's rim, with point intensity color-coded.

To further validate the generality of our method, we evaluate it on two custom-collected datasets designed to test sensor diversity (see Fig. 10): (1) A pinhole camera (Orbbec RGBD) paired with a solid-state LiDAR (Livox Mid360), and (2) A fisheye camera (Insta360 ONE RS) paired with a mechanical LiDAR (HESAI XT32). For both configurations, we used a custom-designed target with reflective circular patterns. The precise reprojection results, shown in Fig. 9c and Fig. 9d, demonstrate that our method is sensor-agnostic, handling both pinhole/fisheye cameras and solid-state/mechanical LiDARs.

Across all scenarios—spanning engineered boards, natural

objects, and diverse sensor models—our method achieves visually consistent and geometrically coherent alignment. This confirms its robustness to sensor type, target design, and environmental complexity.

V. CONCLUSIONS

In this work, we identified and addressed the “Circle Center Problem,” a fundamental yet overlooked bottleneck in high-precision, target-based LiDAR-camera calibration. We demonstrated that conventional pipelines fail due to two critical limitations: (i) inaccurate 3D center estimation from decoupled plane and circle fitting, and (ii) systematic 2D projection errors from erroneously assuming the ellipse center equals the projected 3D center.

To resolve these issues, we proposed a principled framework with two core innovations. First, we used Conformal Geometric Algebra (CGA) to formulate 3D circle fitting as a linear eigenvalue problem. This allows for direct geometric distance minimization and seamless RANSAC integration for robustness. Second, we introduced a chord-length variance minimization method to recover the true 2D projected center. We resolved its inherent dual-minima ambiguity using a robust dual strategy: homography-based validation (for co-planar targets) or a quasi-RANSAC fallback when such geometry is absent.

Extensive experiments on synthetic and real-world datasets, including comparisons against SOTA methods, validated the superiority of our approach. Our method achieved lower 3D center estimation error, reduced reprojection error, and improved extrinsic estimation accuracy. Qualitative results further confirmed robust alignment across diverse scenarios.

This work advances target-based calibration and provides a reliable foundation for training and validating targetless methods. Our code will be publicly released to support reproducibility and benefit the robotics community.

ACKNOWLEDGMENTS

We are deeply grateful to Prof. Yu Zhang, Changjian Jiang, and Zeyu Wan of Zhejiang University for providing the Insta

and LiDAR equipment critical for our field experiments. We also thank Yiming Zhu for his valuable efforts during the execution of the experiments.

REFERENCES

- [1] Y. Li, A. W. Yu *et al.*, “Deepfusion: Lidar-camera deep fusion for multi-modal 3d object detection,” in *Proceedings of the IEEE/CVF conference on computer vision and pattern recognition*, 2022, pp. 17 182–17 191. [1](#)
- [2] X. Bai, Z. Hu, X. Zhu, Q. Huang, Y. Chen, H. Fu, and C.-L. Tai, “Transfusion: Robust lidar-camera fusion for 3d object detection with transformers,” in *Proceedings of the IEEE/CVF conference on computer vision and pattern recognition*, 2022, pp. 1090–1099. [1](#)
- [3] Z. Zhuang, R. Li, K. Jia, Q. Wang, Y. Li, and M. Tan, “Perception-aware multi-sensor fusion for 3d lidar semantic segmentation,” in *Proceedings of the IEEE/CVF international conference on computer vision*, 2021, pp. 16 280–16 290. [1](#)
- [4] T. Shan, B. Englot, C. Ratti, and R. Daniela, “Lvi-sam: Tightly-coupled lidar-visual-inertial odometry via smoothing and mapping,” in *IEEE International Conference on Robotics and Automation (ICRA)*. IEEE, 2021, pp. 5692–5698. [1](#)
- [5] A. Geiger, F. Moosmann, Ö. Car, and B. Schuster, “Automatic camera and range sensor calibration using a single shot,” in *2012 IEEE international conference on robotics and automation*. IEEE, 2012, pp. 3936–3943. [1, 2](#)
- [6] L. F. T. Fu, N. Chebrolu, and M. Fallon, “Extrinsic calibration of camera to lidar using a differentiable checkerboard model,” in *2023 IEEE/RSJ International Conference on Intelligent Robots and Systems (IROS)*, 2023, pp. 1825–1831. [1, 2](#)
- [7] L. Zhou, Z. Li, and M. Kaess, “Automatic extrinsic calibration of a camera and a 3d lidar using line and plane correspondences,” in *2018 IEEE/RSJ International Conference on Intelligent Robots and Systems (IROS)*, 2018, pp. 5562–5569. [1, 2](#)
- [8] J. Kümmelre, T. Kühner, and M. Lauer, “Automatic calibration of multiple cameras and depth sensors with a spherical target,” in *2018 IEEE/RSJ International Conference on Intelligent Robots and Systems (IROS)*, 2018, pp. 1–8. [1, 2](#)
- [9] G. Zhang, K. Wu, J. Lin, T. Wang, and Y. Liu, “Automatic extrinsic parameter calibration for camera-lidar fusion using spherical target,” *IEEE Robotics and Automation Letters*, vol. 9, no. 6, pp. 5743–5750, 2024. [1, 2](#)
- [10] T. Tóth, Z. Pusztai, and L. Hajder, “Automatic lidar-camera calibration of extrinsic parameters using a spherical target,” in *2020 IEEE International Conference on Robotics and Automation (ICRA)*, 2020, pp. 8580–8586. [1, 2](#)
- [11] V. Fremont, S. Rodriguez Florez, and P. Bonnifait, “Circular targets for 3d alignment of video and lidar sensors,” *Advanced Robotics*, vol. 0, pp. 1–27, 12 2012. [1, 2, 3](#)
- [12] Y. Xie, L. Deng, T. Sun, Y. Fu, J. Li, X. Cui, H. Yin, S. Deng, J. Xiao, and B. Chen, “A4lidartag: Depth-based fiducial marker for extrinsic calibration of solid-state lidar and camera,” *IEEE Robotics and Automation Letters*, vol. 7, no. 3, pp. 6487–6494, 2022. [1, 2, 3, 5](#)
- [13] M. Wei, J.-G. Lu, N. Ye, Z. Zhu, Q. Zhang, and Y. Wang, “A full-lifecycle calibration method for camera and lidar in autonomous driving,” *IEEE Transactions on Instrumentation and Measurement*, vol. 74, pp. 1–17, 2025. [1, 2, 3, 5](#)
- [14] H. Liu, Q. Xu, Y. Huang, Y. Ding, and J. Xiao, “A method for synchronous automated extrinsic calibration of lidar and cameras based on a circular calibration board,” *IEEE Sensors Journal*, vol. 23, no. 20, pp. 25 026–25 035, 2023. [1, 2, 3](#)
- [15] D. Kim, S. Shin, and H. Hwang, “Camera-lidar extrinsic calibration using constrained optimization with circle placement,” *IEEE Robotics and Automation Letters*, vol. 10, no. 2, pp. 883–890, 2025. [1, 2, 3, 5](#)
- [16] C. Zheng and F. Zhang, “Fast-calib: Lidar-camera extrinsic calibration in one second,” *arXiv preprint arXiv:2507.17210*, 2025. [1, 2, 3, 8, 9](#)
- [17] J. Domhof, J. F. Kooij, and D. M. Gavrila, “An extrinsic calibration tool for radar, camera and lidar,” in *2019 International Conference on Robotics and Automation (ICRA)*, 2019, pp. 8107–8113. [1, 2, 3](#)
- [18] J. Beltrán, C. Guindel, A. de la Escalera, and F. García, “Automatic extrinsic calibration method for lidar and camera sensor setups,” *IEEE Transactions on Intelligent Transportation Systems*, vol. 23, no. 10, pp. 17 677–17 689, 2022. [1, 2, 3, 8](#)
- [19] G. Yan, F. He, C. Shi, P. Wei, X. Cai, and Y. Li, “Joint camera intrinsic and lidar-camera extrinsic calibration,” in *2023 IEEE International Conference on Robotics and Automation (ICRA)*, 2023, pp. 11 446–11 452. [1, 2, 3](#)
- [20] X. Li, F. He, S. Li, Y. Zhou, C. Xia, and X. Wang, “Accurate and automatic extrinsic calibration for a monocular camera and heterogenous 3d lidars,” *IEEE Sensors Journal*, vol. 22, no. 16, pp. 16 472–16 480, 2022. [1, 3](#)
- [21] S. Wang, S. Zhang, and X. Qiu, “P2o-calib: Camera-lidar calibration using point-pair spatial occlusion relationship,” in *2023 IEEE/RSJ International Conference on Intelligent Robots and Systems (IROS)*, 2023, pp. 1840–1847. [1](#)
- [22] C. Yuan, X. Liu, X. Hong, and F. Zhang, “Pixel-level extrinsic self calibration of high resolution lidar and camera in targetless environments,” *IEEE Robotics and Automation Letters*, vol. 6, no. 4, pp. 7517–7524, 2021. [1, 2](#)
- [23] J. Levinson and S. Thrun, “Automatic online calibration of cameras and lasers,” in *Robotics: science and systems*, vol. 2, no. 7. Berlin, Germany, 2013. [1, 2](#)
- [24] Z. Lin, Z. Gao, X. Liu, J. Wang, W. Song, B. M. Chen, C. Li, Y. Huang, and Y. Zhu, “Sgcalib: A two-stage camera-lidar calibration method using semantic information and geometric features,” in *2024 IEEE International Conference on Robotics and Automation (ICRA)*, 2024, pp. 14 527–14 533. [1, 2](#)
- [25] Y. Zhu, C. Li, and Y. Zhang, “Online camera-lidar calibration with sensor semantic information,” in *2020 IEEE International Conference on Robotics and Automation (ICRA)*. IEEE, 2020, pp. 4970–4976. [1, 2](#)
- [26] G. Pandey, J. McBride, S. Savarese, and R. Eustice, “Automatic targetless extrinsic calibration of a 3d lidar and camera by maximizing mutual information,” *Proceedings of the AAAI Conference on Artificial Intelligence*, vol. 26, no. 1, pp. 2053–2059, Sep. 2021. [1, 2](#)
- [27] Z. Liu, H. Tang, S. Zhu, and S. Han, “Semalign: Annotation-free camera-lidar calibration with semantic alignment loss,” in *2021 IEEE/RSJ International Conference on Intelligent Robots and Systems (IROS)*. IEEE, 2021, pp. 8845–8851. [1, 2](#)
- [28] Z. Luo, G. Yan, X. Cai, and B. Shi, “Zero-training lidar-camera extrinsic calibration method using segment anything model,” in *2024 IEEE International Conference on Robotics and Automation (ICRA)*, 2024, pp. 14 472–14 478. [1, 2](#)
- [29] Z. Taylor and J. Nieto, “Motion-based calibration of multimodal sensor extrinsics and timing offset estimation,” *IEEE Transactions on Robotics*, vol. 32, no. 5, pp. 1215–1229, 2016. [1, 2](#)
- [30] J. Moravec and R. Šára, “Online camera-lidar calibration monitoring and rotational drift tracking,” *IEEE Transactions on Robotics*, vol. 40, pp. 1527–1545, 2024. [1, 2](#)
- [31] J. Zhu, J. Xue, and P. Zhang, “Calibdepth: Unifying depth map representation for iterative lidar-camera online calibration,” in *2023 IEEE International Conference on Robotics and Automation (ICRA)*, 2023, pp. 726–733. [1, 2](#)
- [32] Y. Xiao, Y. Li, C. Meng, X. Li, J. Ji, and Y. Zhang, “Calibformer: A transformer-based automatic lidar-camera calibration network,” in *2024 IEEE International Conference on Robotics and Automation (ICRA)*, 2024, pp. 16 714–16 720. [1, 2](#)
- [33] X. Jing, X. Ding, R. Xiong, H. Deng, and Y. Wang, “Dxq-net: Differentiable lidar-camera extrinsic calibration using quality-aware flow,” in *2022 IEEE/RSJ International Conference on Intelligent Robots and Systems (IROS)*, 2022, pp. 6235–6241. [1, 2](#)
- [34] D. Cattaneo and A. Valada, “Cmrnext: Camera to lidar matching in the wild for localization and extrinsic calibration,” *IEEE Transactions on Robotics*, vol. 41, pp. 1995–2013, 2025. [1, 2](#)
- [35] S. Zhou, S. Xie, R. Ishikawa, and T. Oishi, “Robust lidar-camera calibration with 2d gaussian splatting,” *IEEE Robotics and Automation Letters*, vol. 10, no. 5, pp. 4674–4681, 2025. [1, 2](#)
- [36] Q. Herau, M. Bennehar, A. Moreau, N. Piasco, L. Roldão, D. Tsishkou, C. Mignot, P. Vasseur, and C. Demonceaux, “3dgs-calib: 3d gaussian splatting for multimodal spatiotemporal calibration,” in *2024 IEEE/RSJ International Conference on Intelligent Robots and Systems (IROS)*, 2024, pp. 8315–8321. [1, 2](#)
- [37] R. B. Rusu and S. Cousins, “3D is here: Point Cloud Library (PCL),” in *IEEE International Conference on Robotics and Automation (ICRA)*. Shanghai, China: IEEE, May 9–13 2011. [1, 6](#)
- [38] L. Dorst, “Total least squares fitting of k-spheres in n-d euclidean space using an (n+2)-d isometric representation,” *Journal of Mathematical Imaging and Vision*, vol. 50, 11 2014. [1, 2, 4](#)
- [39] J. Heikkilä, “Geometric camera calibration using circular control points,” *IEEE Transactions on Pattern Analysis and Machine Intelligence*, vol. 22, no. 10, pp. 1066–1077, 2000. [1](#)
- [40] M. Vélez, M. Spaněl, Z. Materna, and A. Herout, “Calibration of rgb camera with velodyne lidar,” in *Proc. Int. Conf. Comput. Graph., Visualizat. Comput. Vis.*, vol. 2014, no. 22, 2014, pp. 135–144. [1, 2](#)

- [41] J.-S. Kim, P. Gurdjos, and I.-S. Kweon, “Geometric and algebraic constraints of projected concentric circles and their applications to camera calibration,” *IEEE Transactions on Pattern Analysis and Machine Intelligence*, vol. 27, no. 4, pp. 637–642, 2005. [2](#), [5](#)
- [42] D. Cucci, “Accurate optical target pose determination for applications in aerial photogrammetry,” *ISPRS Annals of the Photogrammetry, Remote Sensing and Spatial Information Sciences*, vol. 3, pp. 257–262, 2016. [2](#), [5](#)
- [43] A. Geiger, P. Lenz, and R. Urtasun, “Are we ready for autonomous driving? the kitti vision benchmark suite,” in *Conference on Computer Vision and Pattern Recognition (CVPR)*, 2012. [2](#)
- [44] V. Pătrăucean, P. Gurdjos, and R. G. Von Gioi, “A parameterless line segment and elliptical arc detector with enhanced ellipse fitting,” in *Eur. Conf. Comput. Vis.* Springer, 2012, pp. 572–585. [3](#)
- [45] C. Meng, Z. Li, X. Bai, and F. Zhou, “Arc adjacency matrix-based fast ellipse detection,” *IEEE Trans. Image Process.*, vol. 29, pp. 4406–4420, 2020. [3](#)
- [46] R. A. McLaughlin, “Randomized hough transform: improved ellipse detection with comparison,” *Pattern Recognit. Lett.*, vol. 19, no. 3-4, pp. 299–305, 1998. [3](#)
- [47] G. Bradski, “The OpenCV Library,” *Dr. Dobb's Journal of Software Tools*, 2000. [3](#)
- [48] C. Lu, S. Xia, M. Shao, and Y. Fu, “Arc-support line segments revisited: An efficient high-quality ellipse detection,” *IEEE Trans. Image Process.*, vol. 29, pp. 768–781, 2019. [3](#)
- [49] M. A. Fischler and R. C. Bolles, “Random sample consensus: a paradigm for model fitting with applications to image analysis and automated cartography,” *Commun. ACM*, vol. 24, pp. 381–395, 1981. [Online]. Available: <https://api.semanticscholar.org/CorpusID:972888> [4](#)
- [50] L. Hongbo, H. David, and A. Rockwood, “Generalized homogeneous coordinates for computational geometry,” in *Geometric Computing with Clifford Algebras*. Springer, 06 2001, pp. 27–59. [4](#)
- [51] R. Hartley, “In defense of the eight-point algorithm,” *IEEE Transactions on Pattern Analysis and Machine Intelligence*, vol. 19, no. 6, pp. 580–593, 1997. [4](#)
- [52] D. Nister, “An efficient solution to the five-point relative pose problem,” *IEEE Transactions on Pattern Analysis and Machine Intelligence*, vol. 26, no. 6, pp. 756–770, 2004. [4](#)
- [53] L. Calvet, P. Gurdjos, C. Griwodz, and S. Gasparini, “Detection and accurate localization of circular fiducials under highly challenging conditions,” in *2016 IEEE Conference on Computer Vision and Pattern Recognition (CVPR)*, 2016, pp. 562–570. [5](#)
- [54] N. Koenig and A. Howard, “Design and use paradigms for gazebo, an open-source multi-robot simulator,” in *2004 IEEE/RSJ international conference on intelligent robots and systems (IROS)(IEEE Cat. No. 04CH37566)*, vol. 3. Ieee, 2004, pp. 2149–2154. [8](#)
- [55] F. Chen, L. Li, S. Zhang, J. Wu, and L. Wang, “Pbacalib: Targetless extrinsic calibration for high-resolution lidar-camera system based on plane-constrained bundle adjustment,” *IEEE Robotics and Automation Letters*, vol. 8, no. 1, pp. 304–311, 2022. [8](#), [9](#)